JGR Solid Earth

RESEARCH ARTICLE

10.1029/2019JB017851

Key Points:
- The differential equations of dynamic thermoporoelasticity are solved with a direct grid method
- The solver is based on the Fourier pseudospectral method to compute the spatial derivatives
- The simulation reveals the behavior of four wave modes, namely, the fast P, slow P, S, and the thermal wave-diffusion field

Supporting Information:
- Supporting Information S1
- Movie S1
- Movie S2

Correspondence to:
J. Ba,
jingba@188.com

Citation:
Carcione, J. M., Cavallini, F., Wang, E., Ba, J., & Fu, L.-Y. (2019). Physics and simulation of wave propagation in linear thermoporoelastic media. *Journal of Geophysical Research: Solid Earth*, *124*, 8147–8166. https://doi.org/10.1029/2019JB017851

Received 16 APR 2019
Accepted 28 JUN 2019
Accepted article online 4 JUL 2019
Published online 20 AUG 2019
Corrected 22 JUL 2020

This article was corrected on 22 JUL 2020. See the end of the full text for details.

Physics and Simulation of Wave Propagation in Linear Thermoporoelastic Media

José M. Carcione[1,2], Fabio Cavallini[1], Enjiang Wang[2], Jing Ba[2], and Li-Yun Fu[3]

[1]Istituto Nazionale di Oceanografia e di Geofisica Sperimentale, Sgonico, Italy, [2]School of Earth Sciences and Engineering, Hohai University, Nanjing, China, [3]School of Geosciences, China University of Petroleum (East China), Qingdao, China

Abstract We develop a numerical algorithm for simulation of wave propagation in linear nonisothermal poroelastic media, based on Biot theory and a generalized Fourier law of heat transport in analogy with Maxwell model of viscoelasticity. A plane wave analysis indicates the presence of the classical *P* and *S* waves and two slow waves, namely, the Biot and the thermal slow modes of propagation, which present diffusive behavior under certain conditions, depending on viscosity, frequency, and the thermoelastic constants. The wavefield is computed with a direct meshing method using the Fourier differential operator to calculate the spatial derivatives. We propose two alternative time-stepping algorithms, namely, a first-order explicit Crank-Nicolson method and a second-order splitting method. The Fourier differential operator provides spectral accuracy in the calculation of the spatial derivatives. Modeling the thermal diffusive mode is relevant for high-temperature high-pressure fields and since it leads to mesoscopic attenuation by mode conversion of the fast waves to the thermal waves.

1. Introduction

The theory of thermoporoelasticity combines the equation of heat conduction with Biot's equations of poroelasticity; specifically, it describes the coupling between the fields of deformation and temperature. The theory is relevant for geophysical studies such as seismic attenuation (Armstrong, 1984; Treitel, 1959) and geothermal and hydrocarbon exploration in general (e.g, Fu, 2012, 2017; Jacquey et al., 2015).

The heat equation is generalized in analogy with Maxwell model of viscoelasticity (Carcione, Poletto et al. 2018). Biot (1956) used differential equations based on the classical heat conduction, but this formulation has unphysical solutions such as discontinuities and infinite velocities as a function of frequency. The generalization to finite velocities is usually termed Lord-Shulman model (Lord & Shulman, 1967; Reza Eslami et al., 2013), but the hyperbolic heat transfer equation, which contains a relaxation time, has been used before by Maxwell (1867), Vernotte (1948), and Cattaneo (1958), leading to a Maxwell-type mechanical model kernel and converting the thermal diffusion to wave-like propagation (finite speeds) at high frequencies. Regarding nonporous thermoelasticity, Rudgers (1990) analyzed the physics and Carcione, Poletto et al. (2018) provided further insight into the physics and solved the wave propagation problem with a direct grid-meshing-numerical method based on the Fourier pseudospectral operator to compute the spatial derivatives.

The theory of wave propagation in porous media has been developed by Maurice A. Biot (Biot, 1962; Carcione, 2014). He considered a matrix (skeleton or frame) fully saturated with a fluid and predicted the existence of two compressional (*P*) waves and a shear wave. The second *P* wave (Biot wave) is diffusive at low frequencies and has a lower velocity than that of the fast *P* wave at high frequencies. The diffusive behavior is not present if the fluid viscosity is 0 or the frame permeability is infinite. Biot (1962) assumes a continuum mechanics approach applied to measurable macroscopic quantities, ignoring the detailed geometrical features of the microscopic elements of the medium (mineral grains, pores, and grain contacts). The theory is quite general, since it does not make any assumption on the shape and geometry of the pores and grains.

The constitutive equations of the theory of porothermoelasticity involve the coupling of the stress components with the temperature field (Noda, 1990; Nield & Bejan, 2006). The dynamical equations predict four propagation modes, namely, a fast *P* or *E* (elastic) wave, a slow (Biot) diffusion/wave, a slow *T* (thermal) diffusion/wave, and a shear wave (e.g., Sharma, 2008). The thermal mode is diffusive for low values

10.1029/2019JB017851

of the thermal conductivity and wave-like for high values of this property. Compared to the uncoupled case (isothermal case), the velocity of the fast P wave is higher and the S wave is not affected by the thermal effects.

Iesan and Quintanilla (2014) derive a theory of porothermoelasticity, based on a double porosity structure. This theory is not based on Biot equations and Darcy law, so that it is not directly comparable with ours. Kumar et al. (2017) performed a plane wave analysis and found four coupled P waves, namely, the P wave, a thermal wave, a so-called longitudinal volume fractional wave corresponding to the pores (first porosity), and a longitudinal volume fractional wave corresponding to the "fissures" (second porosity), in addition to an S wave which is not affected by the thermal properties. The last two P waves are possibly slow waves of the Biot type, but the authors do not provide such identification and/or analysis of the physics, Moreover, Kumar et al. (2017) predict negative quality factors, which suggest that the propagation can be unstable.

We solve the thermoporoelasticity equations by using the Fourier method to compute the spatial derivatives (e.g., Carcione, 2014) and two explicit time integration techniques. The differential equations are stiff, meaning that there are large negative eigenvalues of the system of equations due to the Biot wave and to the Maxwell relaxation time in the heat equation, while the eigenvalues of the fast waves have a small real part. A splitting or partition method solves this problem by calculating the unstable part of the equations analytically. The equations of motion are solved with a Crank-Nicolson time-stepping method. Alternatively, a Runge-Kutta time integration technique to solve the nonstiff part of the differential equations is also implemented (Carcione & Quiroga-Goode, 1995; Carcione, Poletto et al. 2018).

As conventional sources of hydrocarbons decline, the exploration is being started to be developed in unexplored or underdeveloped areas. High-pressure high-temperature reservoirs are increasingly becoming the focus of petroleum exploration in the search for additional reserves. The modeling method developed in this work can be relevant for the exploration of high-pressure high-temperature deep reservoirs and tight oil and gas resources in thermal hydrocarbon source rocks with temperatures above 400 °C (e.g., Fu, 2012, 2017), as well as in geothermal fields (Bonafede, 1991; Carcione, Wang et al. 2018).

2. Equations of Motion

Let us define by v_i and q_i, $i = 1, 2$, the components of the particle velocity fields of the frame and fluid relative to the frame, respectively, σ_{ij} the components of the *total* (bulk) stress tensor, p the fluid pressure, and T the increment of temperature above a reference absolute temperature T_0 for the state of zero stress and strain. To obtain the equations of dynamic thermoporoelasticity in 2-D isotropic media, we generalize the equations given in Carcione, Poletto et al. (2018) to the poroelastic case (e.g., Carcione, 1996, 2014). We have the following constitutive equations:

$$\begin{aligned}
\dot{\sigma}_{xx} &= 2\mu v_{x,x} + \lambda \epsilon_m + \alpha M \epsilon - \beta \dot{T} + f_{xx}, \\
\dot{\sigma}_{zz} &= 2\mu v_{z,z} + \lambda \epsilon_m + \alpha M \epsilon - \beta \dot{T} + f_{zz}. \\
\dot{\sigma}_{xz} &= \mu(v_{x,z} + v_{z,x}) + f_{xz}, \\
\dot{\sigma}_f &= -\phi \dot{p} = \phi M \epsilon - \beta_f \dot{T} + f_f, \\
\epsilon &= \alpha \epsilon_m + \epsilon_f, \quad \epsilon_m = v_{x,x} + v_{z,z}, \quad \epsilon_f = q_{x,x} + q_{z,z},
\end{aligned} \tag{1}$$

where f_{xx}, f_{zz}, f_{xz}, and f_f are external sources, respectively. The subscript ", i" denotes the spatial derivative $\partial/\partial x_i$, and a dot above a variable indicates a time derivative. The notation here is such that the rate of variation of fluid content is $\dot{\zeta} = -q_{i,i}$ (Carcione, 2014). In the following, the subscripts "m" and "f" refer to the solid (dry) matrix and the fluid, respectively.

The elastic and thermal coefficients are as the following: λ is the Lamé constant of the drained matrix, μ is the shear modulus of the drained (and saturated) matrix,

$$\begin{aligned}
M &= \frac{K_s}{1 - \phi - K_m/K_s + \phi K_s/K_f}, \\
\alpha &= 1 - \frac{K_m}{K_s}, \\
K_m &= \lambda + \frac{2}{3}\mu,
\end{aligned} \tag{2}$$

with K_s and K_f the solid and fluid bulk moduli, respectively; ϕ is the porosity, and β and β_f the coefficients of thermoelasticity of the bulk material and fluid, respectively.

Dynamical equations

$$
\begin{aligned}
&\sigma_{xx,x} + \sigma_{xz,z} = \rho \dot{v}_x + \rho_f \dot{q}_x + f_x, \\
&\sigma_{xz,x} + \sigma_{zz,z} = \rho \dot{v}_z + \rho_f \dot{q}_z + f_z, \\
&-p_{,x} = \rho_f \dot{v}_x + m \dot{q}_x + \frac{\eta}{\kappa} q_x, \\
&-p_{,z} = \rho_f \dot{v}_z + m \dot{q}_z + \frac{\eta}{\kappa} q_z, \\
&\Delta_\gamma T = c(\dot{T} + \tau \ddot{T}) + \beta T_0 \left[(\epsilon_m + \tau \dot{\epsilon}_m) + (\epsilon_f + \tau \dot{\epsilon}_f) \right] + q,
\end{aligned}
\tag{3}
$$

where

$$\Delta_\gamma = (\gamma T_{,x})_{,x} + (\gamma T_{,z})_{,z} \tag{4}$$

(Dhaliwal & Sherief, 1980),

$$\rho = (1 - \phi)\rho_s + \phi \rho_f \tag{5}$$

is the composite density, with ρ_s and ρ_f the solid and fluid densities, respectively; $m = \mathcal{T} \rho_f / \phi$, with $\mathcal{T}$ the tortuosity; η is the fluid viscosity; κ is the permeability of the medium; γ is the bulk coefficient of heat conduction (or thermal conductivity); c is the bulk specific heat of the unit volume in the absence of deformation; τ is a Maxwell-Vernotte-Cattaneo relaxation time; f_i are external forces; q is a heat source; and $\Delta_\gamma = \gamma \Delta$ in the homogeneous case, with Δ the Laplacian. These equations assume thermal equilibrium between the solid and the fluid; that is, the temperature in both phases is the same. Thermal equilibrium is valid when the interstitial heat transfer coefficient between the solid and fluid is very large and the ratio of pore surface area to pore volume is sufficiently high.

Next, we compare our equations with other formulations presented in the literature. Biot (1956) and Deresiewicz (1957) do not consider the relaxation term, leading to unphysical results (see Carcione, Poletto et al. 2018). McTigue (1986) and Bonafede (1991) treat the static problem, so that there are no inertial terms (accelerations) and no relaxation effects. The heuristic heat equation in equations (3) reduces to that of linear thermoelasticity for a solid (no fluid) and to the heat equation for a fluid, as expected. If one wishes to allow for heat transfer between the solid and the fluid, a starting point to do this is given in Nield and Bejan (2006, equations 2.11 and 2.12), where the inertial terms have to be included (those related to ϵ_m and ϵ_f in equation $(3)_5$). Sharma (2008) obtains similar equations, with $\beta = \beta_m + \alpha \beta_f$, where β_m corresponds to the skeleton or matrix. Noda (1990, equation 6) neglects the inertial terms in the temperature equation but includes the nonlinear advection term. This author relates these coefficients to the coefficients of thermal expansion, α_m and α_f, as $\beta_m = 3[(K_m + (\alpha - \phi)^2 M)\alpha_m + \phi(\alpha - \phi)M\alpha_f]$ and $\beta_f = 3\phi M[(\alpha - \phi)\alpha_m + \phi \alpha_f]$. The behavior of these quantities is such that for $\phi = 0$, $K_m = K_s$, $\alpha = 0$, $\beta_m = 3K_s\alpha_m$, and $\beta_f = 0$, and for $\phi = 1$, $K_m = 0$, $\alpha = 1$, $M = K_f$, $\beta_m = 0$, and $\beta_f = 3K_f\alpha_f$. Here, we consider β, β_f, γ, and c as parameters, obtained from experiments or from a specific theoretical model.

3. Particle Velocity-Stress-Temperature Formulation

We recast the equations as new expressions to be used for the numerical simulation of the fields. Equations (3) yield

$$
\begin{aligned}
\dot{v}_x &= \beta_{11}(\sigma_{xx,x} + \sigma_{xz,z} - f_x) - \beta_{12}\left(p_{,x} + \frac{\eta}{\kappa} q_x\right) \equiv \Pi_x, \\
\dot{v}_z &= \beta_{11}(\sigma_{xz,x} + \sigma_{zz,z} - f_z) - \beta_{12}\left(p_{,z} + \frac{\eta}{\kappa} q_z\right) \equiv \Pi_z, \\
\dot{q}_x &= \beta_{21}(\sigma_{xx,x} + \sigma_{xz,z} - f_x) - \beta_{22}\left(p_{,x} + \frac{\eta}{\kappa} q_x\right) \equiv \Omega_x, \\
\dot{q}_z &= \beta_{21}(\sigma_{xz,x} + \sigma_{zz,z} - f_z) - \beta_{22}\left(p_{,z} + \frac{\eta}{\kappa} q_z\right) \equiv \Omega_z,
\end{aligned}
\tag{6}
$$

where

$$\begin{bmatrix} \beta_{11} & \beta_{12} \\ \beta_{21} & \beta_{22} \end{bmatrix} = ({\rho_f}^2 - \rho m)^{-1} \begin{bmatrix} -m & \rho_f \\ \rho_f & -\rho \end{bmatrix}. \tag{7}$$

10.1029/2019JB017851

Table 1
Medium Properties

Properties	Values
Grain bulk modulus, K_s	35 GPa
density, ρ_s	2,650 kg/m^3
Frame bulk modulus, K_m	1.7 GPa
shear modulus, μ_m	1.885 GPa
porosity, ϕ	0.3
permeability, κ	1 darcy
tortuosity, $\mathcal{T}$	2
Water density, ρ_f	1,000 kg/m^3
viscosity, η_f	0.001 Pa s
bulk modulus, K_f	2.4 GPa
thermoelasticity coefficient, β_f	40,000 kg/(m s^2 °K)
Bulk specific heat, c	820 kg/(m s^2 °K)
thermoelasticity coefficient, β	120,000 kg/(m s^2 °K)
absolute temperature, T_0	300 °K
Case 1	
thermal conductivity, γ	10.5 m kg/(s^3 °K)
relaxation time, τ	1.5×10^{-8} s
Case 2	
thermal conductivity, γ	4.5×10^6 m kg/(s^3 ° K)
relaxation time, τ	1.5×10^{-2} s

Defining

$$\dot{T} = \psi, \tag{8}$$

equation $(3)_5$ becomes

$$\dot{\psi} = (c\tau)^{-1} \left[\Delta_\gamma T - q - \beta T_0(\epsilon_m + \tau(\Pi_{x,x} + \Pi_{z,z}) + \epsilon_f + \tau(\Omega_{x,x} + \Omega_{z,z}))\right] - \frac{1}{\tau}\psi. \tag{9}$$

The system of equations is completed with the constitutive equations (1). A plane wave analysis to obtain the phase velocity and attenuation factor of the wave modes is given in Appendix A.

3.1. The Algorithms

The 2-D velocity-stress differential equations can be written in matrix form as

$$\dot{\mathbf{v}} + \mathbf{s} = \mathbf{M}\mathbf{v}, \tag{10}$$

where

$$\mathbf{v} = [v_x, v_z, q_x, q_z, \sigma_{xx}, \sigma_{zz}, \sigma_{xz}, p, T, \psi]^\top \tag{11}$$

is the unknown array vector,

$$\mathbf{s} = [-\beta_{11} f_x, -\beta_{11} f_z, -\beta_{21} f_x, -\beta_{21} f_z, f_{xx}, f_{zz}, f_{xz}, -f_f/\phi, 0, q']^\top \tag{12}$$

is the source vector, and $\mathbf{M}$ is the propagation matrix containing the spatial derivatives and material properties, where $q' = -(c\tau)^{-1} q$.

The solution to equation (10) subject to the initial condition $\mathbf{v}(0) = \mathbf{v}_0$ is formally given by

$$\mathbf{v}(t) = \exp(t\mathbf{M})\mathbf{v}_0 + \int_0^t \exp(\tau\mathbf{M})\mathbf{s}(t-\tau)\mathrm{d}\tau, \tag{13}$$

where $\exp(t\mathbf{M})$ is called evolution operator.

We solve the equations with the time integration methods given in Appendices B and C. The spatial derivatives are calculated with the Fourier method by using the fast Fourier transform (Carcione, 2014). This spatial approximation is infinitely accurate for band-limited periodic functions with cutoff spatial wavenumbers which are smaller than the cutoff wavenumbers of the mesh.

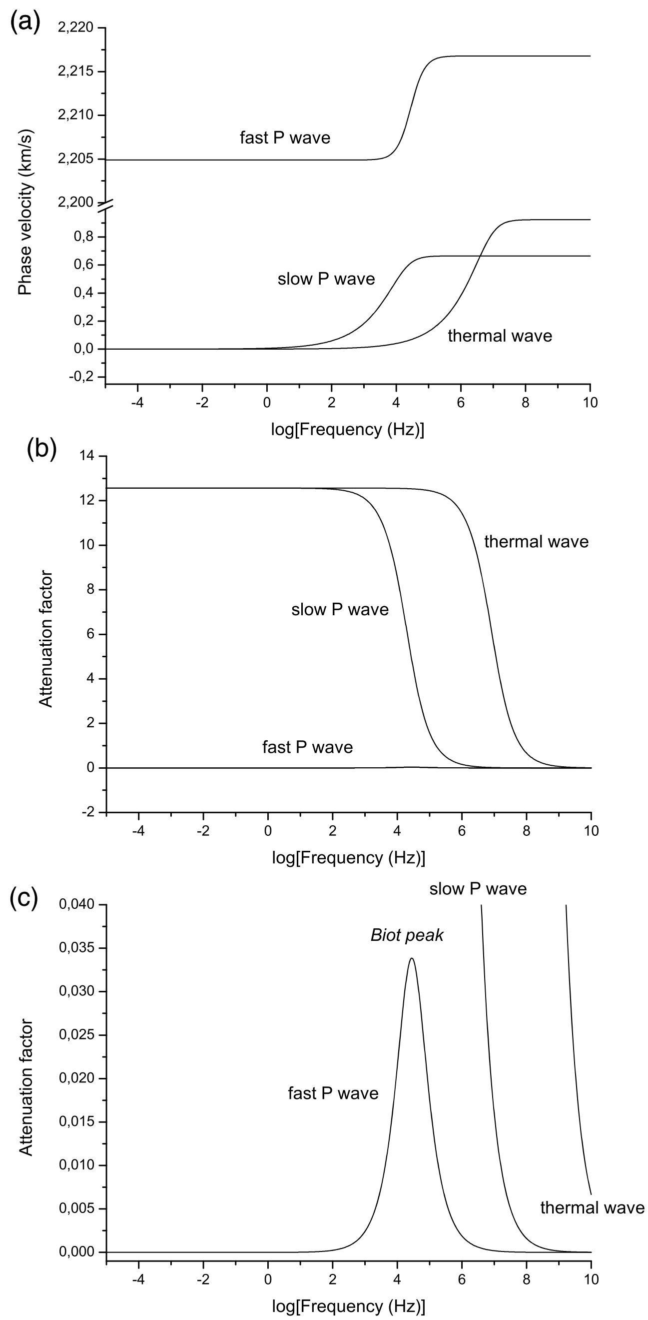

Figure 1. Phase velocity (a) and attenuation factor (L; b and c) as a function of frequency for the uncoupled case ($\beta = \beta_f = \beta_m = 0$). The properties are given in Table 1 (Case 1).

4. Physics and Simulations

We consider the poroelasticity material properties given in Table 1, which are taken from Carcione, (2014; see his Figure 7.9), and two different cases regarding the thermoelasticity properties. The parameters of Case 1 are typical of rocks, while those of Case 2 may refer to a hypothetical synthetic material. Basically, the reason is to show how the physics behaves for different values of the thermal conductivity. Sharma (2008) considers $\gamma = 170$ m kg/(s^3 °K), $c = 2.3 \times 10^6$ kg/(m s^2 °K), $\tau = 10^{-10}$ s, $\beta_f = 0.0003\mu$ °K^{-1}, and $\beta_s = 2\beta_f$. He made plots of wave velocity and attenuation as a function of a parameter $\eta = (\omega\tau)^{-1}$ in the range $0 < \eta < 0.2$, which implies $\omega > 50$ GHz, a frequency range outside of geophysical and rock physics applications (see

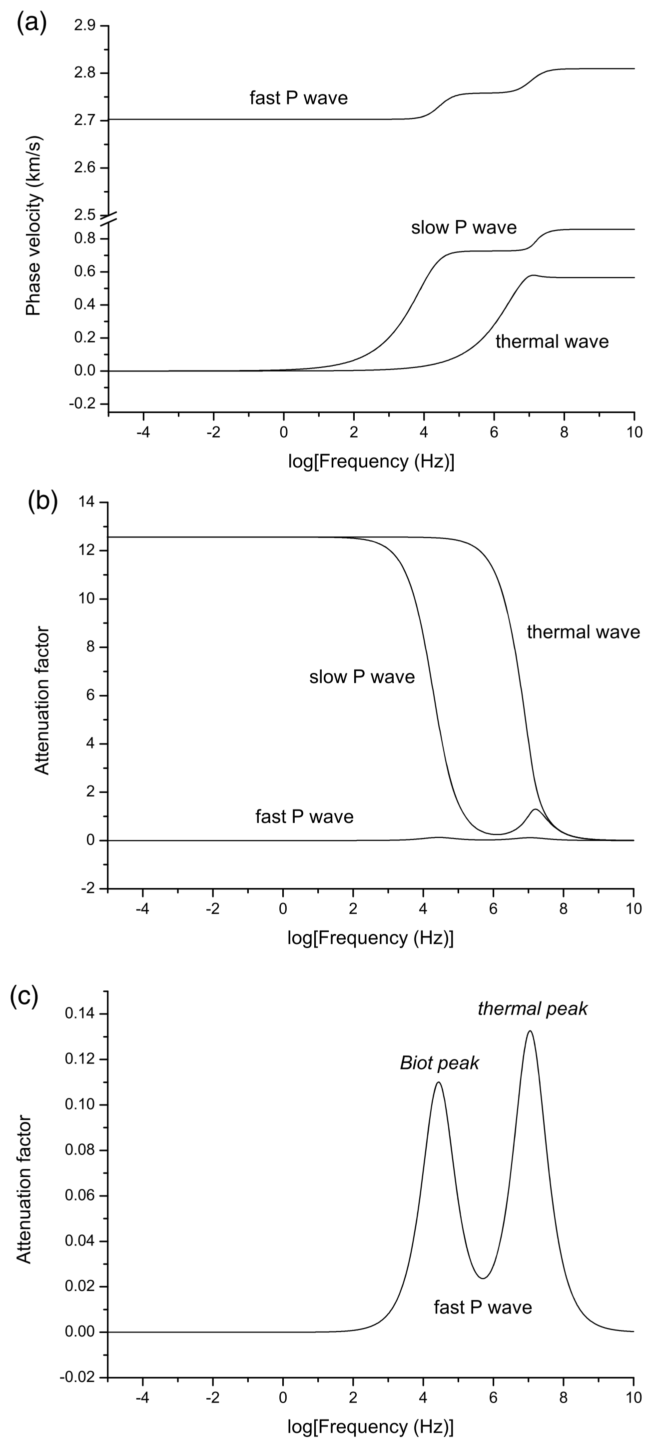

Figure 2. Phase velocity (a) and attenuation factor (b and c) as a function of frequency for the coupled case. The properties are given in Table 1 (Case 1).

his Figure 2). With the above properties, the T wave is diffusive till $\omega = 0.2$ GHz approximately. Here, we consider geophysical meaningful properties.

On the basis of the properties of Table 1, Figure 7.9 of Carcione (2014) shows the phase velocities as a function of frequency for the poroelastic case (uncoupled isothermal case, no thermal effects). Figure 1 displays the phase velocity (A7) (a) and attenuation factor (A8) (b and c; Case 1) when heat conduction and deformation

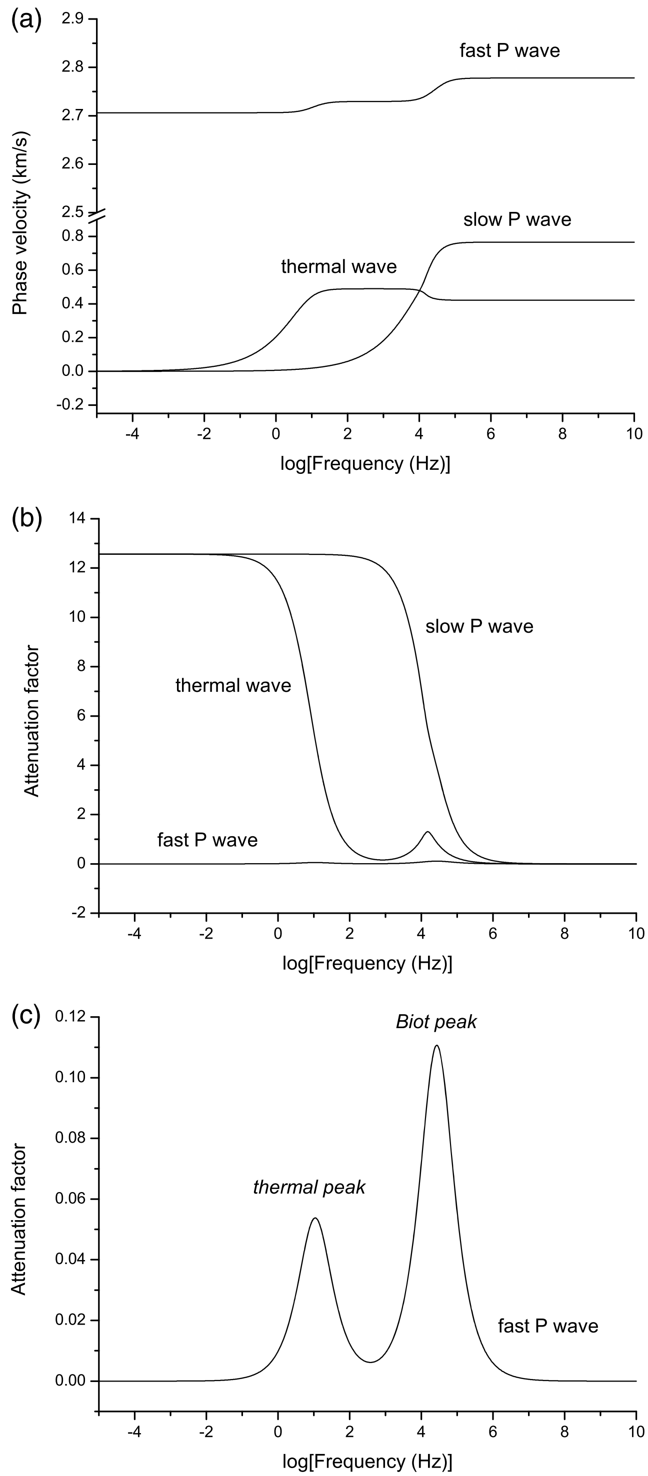

Figure 3. Phase velocity (a) and attenuation factor (b and c) as a function of frequency for the coupled case. The properties are given in Table 1 (Case 2).

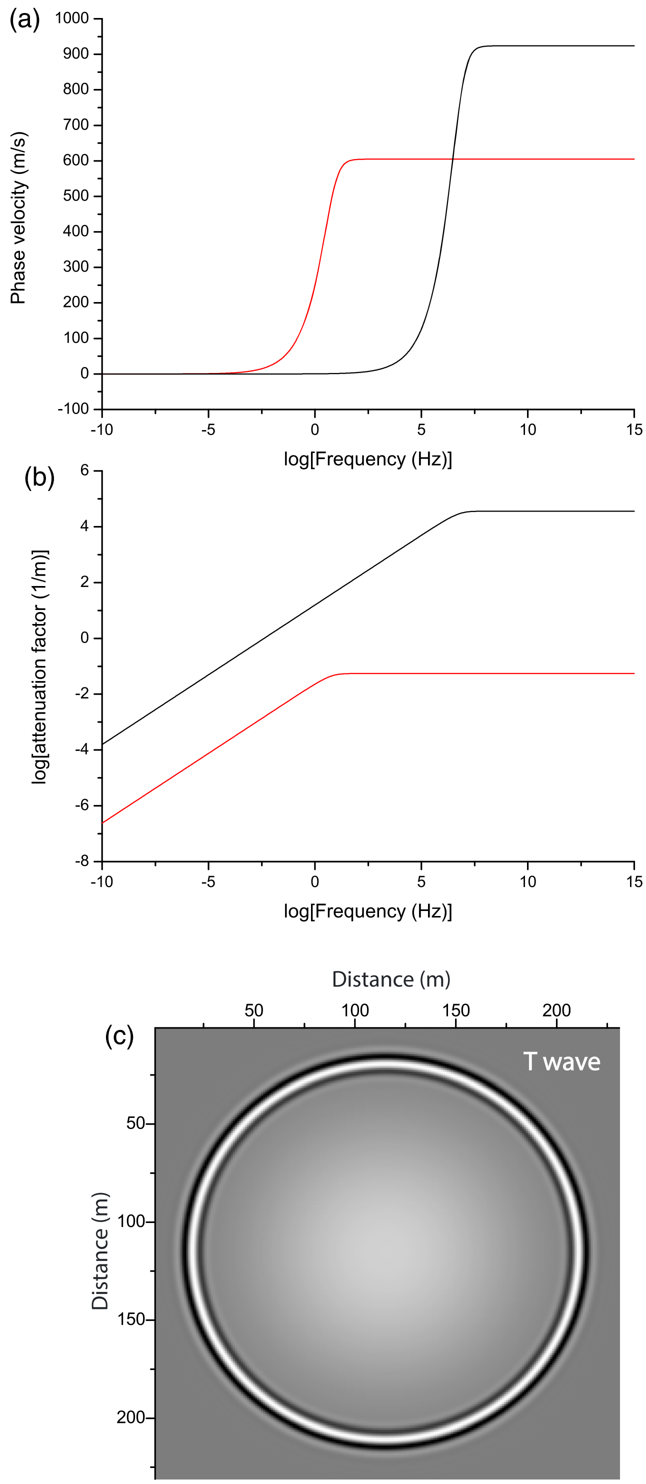

Figure 4. Phase velocity (a), $\log_{10}(A)$ (b), and snapshot of the temperature field at 0.18 s (c) in the uncoupled case. The black line corresponds to Case 1, whereas the red line and the snapshot correspond to Case 2.

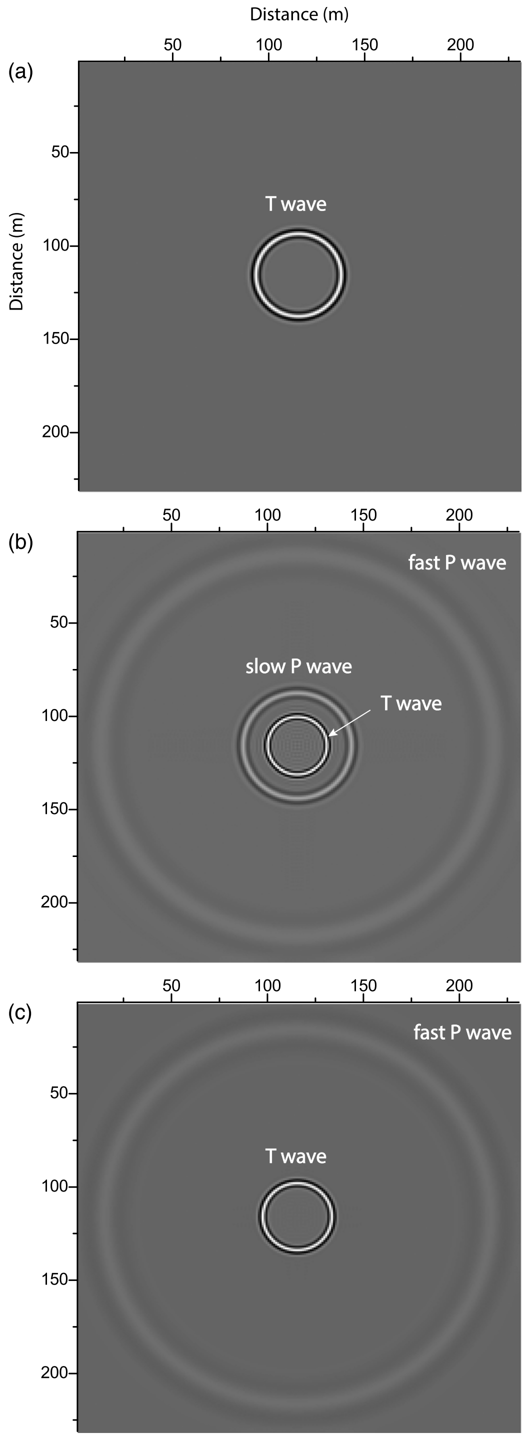

Figure 5. Snapshot of the temperature field T at 47.5 ms in the uncoupled case (a), $\eta = 0$ (b), and $\eta \neq 0$ (c). The last two panels correspond to the coupled case. The sources are dilatational (f_{xx}, f_{zz}, f_f, and q), and the properties are those of Case 2.

are uncoupled. Figures 2 and 3 show the results in the coupled case for Cases 1 and 2, respectively. The plots show that the fast P wave has two Zener-like relaxation peaks, related to the Biot and thermal loss mechanisms. Moreover, the slow and thermal waves are strongly diffusive at low frequencies. For Case 2, the thermal attenuation peak moved to the seismic band and the thermal wave is more wave-like at these frequencies. Kumar et al. (2017), based on the theory of Iesan and Quintanilla (2014), predict negative quality factors of the P wave, in this case, at the whole frequency range, despite the fact that the latter authors have shown the uniqueness of solutions as well as their stability when the internal energy is positive definite. Our attenuation factor is positive over all frequencies.

The following are simulations computed with the Crank-Nicolson algorithm. We obtain snapshots of the wavefield, where we consider a 231 × 231 mesh. The source is located at the center of the mesh and has the time history

$$h(t) = \cos[2\pi(t - t_0)f_0]\exp[-2(t - t_0)^2 f_0^2], \tag{14}$$

where f_0 is the central frequency and $t_0 = 3/(2f_0)$ is a delay time.

The Biot slow P wave and the T wave have a similar behavior at the high and low frequencies, with a diffusive and wave-like behavior, respectively. This behavior also depends on the medium properties. In the uncoupled case ($\beta_m = \beta_f = 0$) and for the values of Case 1, we have $c_\infty = 924$ m/s (thermal wave). On the other hand, we have $c_\infty = 605$ m/s for Case 2. Figure 4 shows the phase velocity (a), $\log_{10}(A)$ (b), and snapshot of the temperature field (c). The black line corresponds to Case 1, whereas the red line and the snapshot correspond to Case 2. We have considered a grid spacing of $dx = dz = 1$ m, $dt = 0.2$ ms, $f_0 = 75$ Hz (a heat source q), and a propagation time of 0.18 s. For Case 1, the T wave does not propagate due to the strong attenuation and the very low phase velocity at the source frequency range.

Next, in all the following experiments, we consider a central frequency of $f_0 = 150$ Hz and run the simulations with $dt = 0.05$ ms. Figure 5 shows snapshots of the temperature field at 47.5 ms in the uncoupled case (a), $\eta = 0$ (b), and $\eta \neq 0$ (c) (Case 2). The last two panels correspond to the coupled case. The sources are dilatational (f_{xx}, f_{zz}, f_f, and q). The same plots for v_z and q_z are shown in Figures 6 and 7, respectively. The slow P and T wavefronts can be seen in the snapshots (see the phase velocities in Figure 3a). (The high-frequency limit velocity of the slow wave can be obtained as a root of the second-order equation (7.329) in Carcione, 2014). As can be seen, the slow wave is diffusive in panel (c). We observe that the fast P wave velocity is higher in the coupled case (compare Figures 6a and 6b), in agreement with Figures 1a and 2a. The same phenomenon was observed in the thermoelastic (nonporous) case, where a detailed analysis has been performed (Carcione, Poletto et al. 2018). Figure 8 shows snapshots using the properties of Case 1, where $\eta = 0$. In this case, the T wave is diffusive and can be seen at the source location. The field generated by a heat source is shown in Figure 9 (Case 2). As can be appreciated, a heat source generates significant elastic wave fields

Figure 10 shows the results for a shear source (f_{xz}) and $\eta = 0$ at a propagation time of 75 ms (Case 2). We have used absorbing boundaries to damp the fast P wave, whose wavefront exceeds the size of the model and undergoes wraparound. The S wave is not coupled to the heat equation, but since a shear source generates P waves in the near field, these signals appear in all the field components, including the temperature field. In particular, we can see the S wave and the two slow waves in panel (c). To complete the analysis of wave

10.1029/2019JB017851

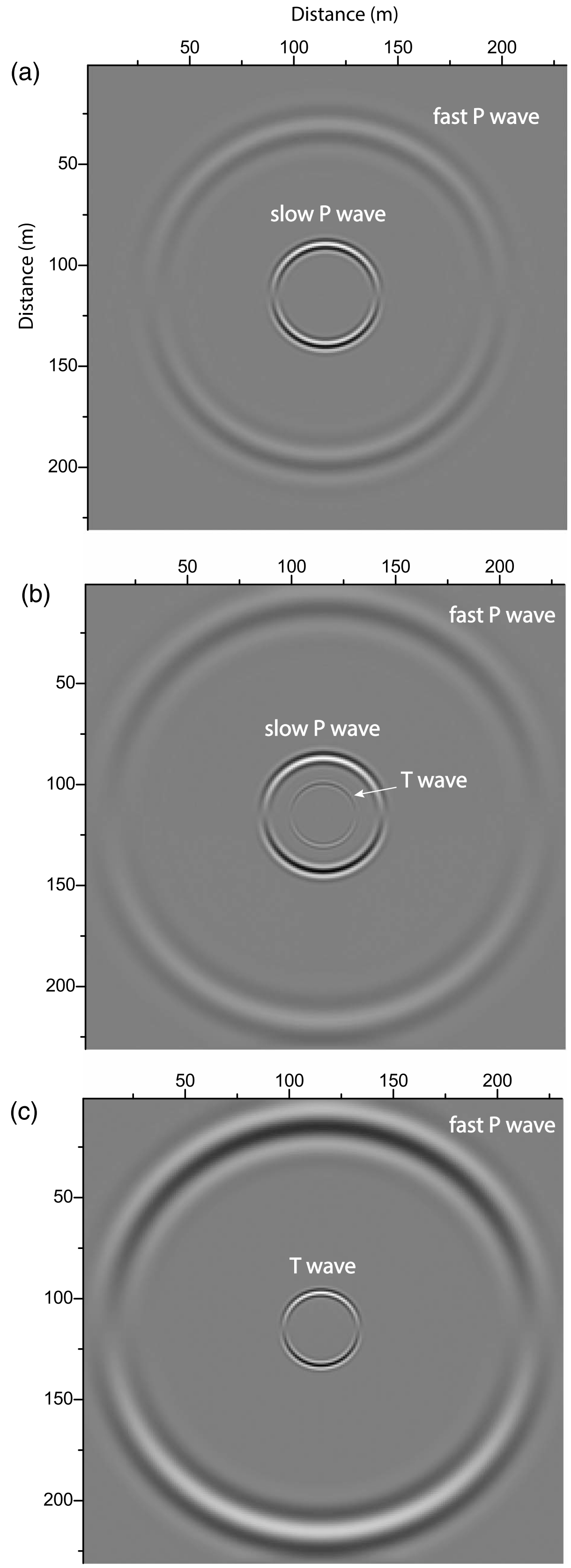

Figure 6. Snapshot of the particle velocity of the frame v_z at 47.5 ms (see caption of Figure 5).

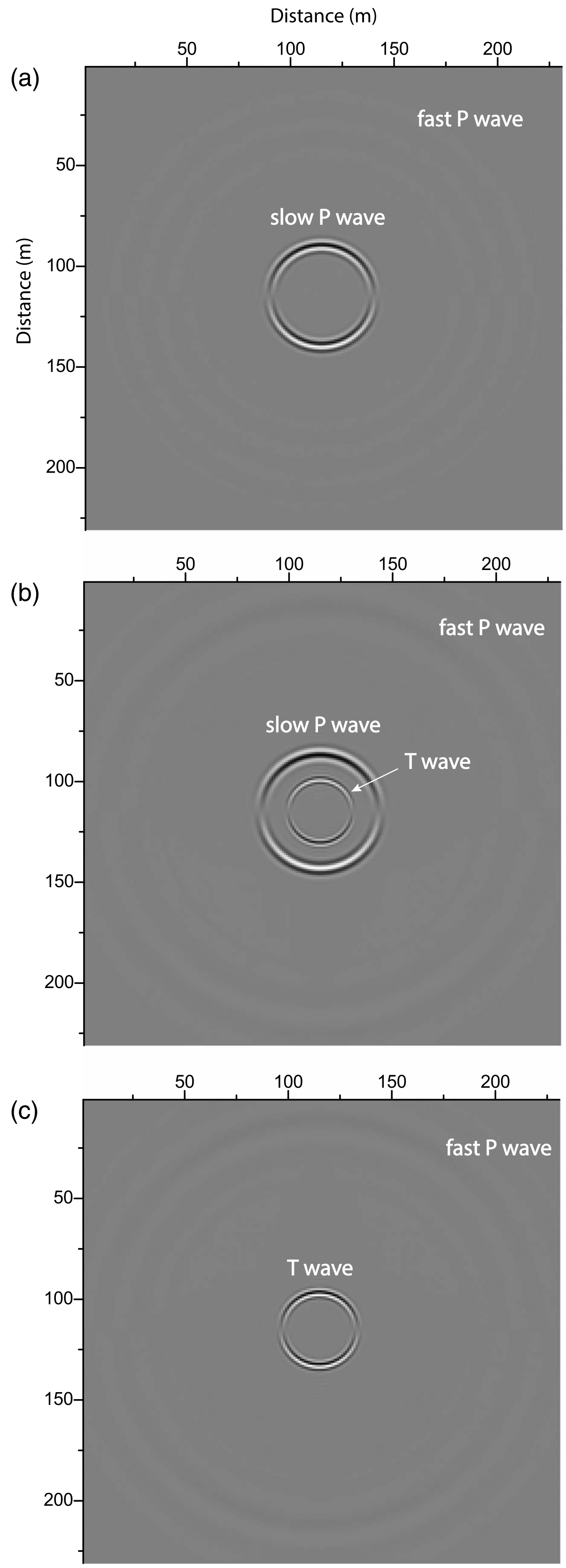

Figure 7. Snapshot of the particle velocity of the fluid relative to the solid q_z at 47.5 ms (see caption of Figure 5).

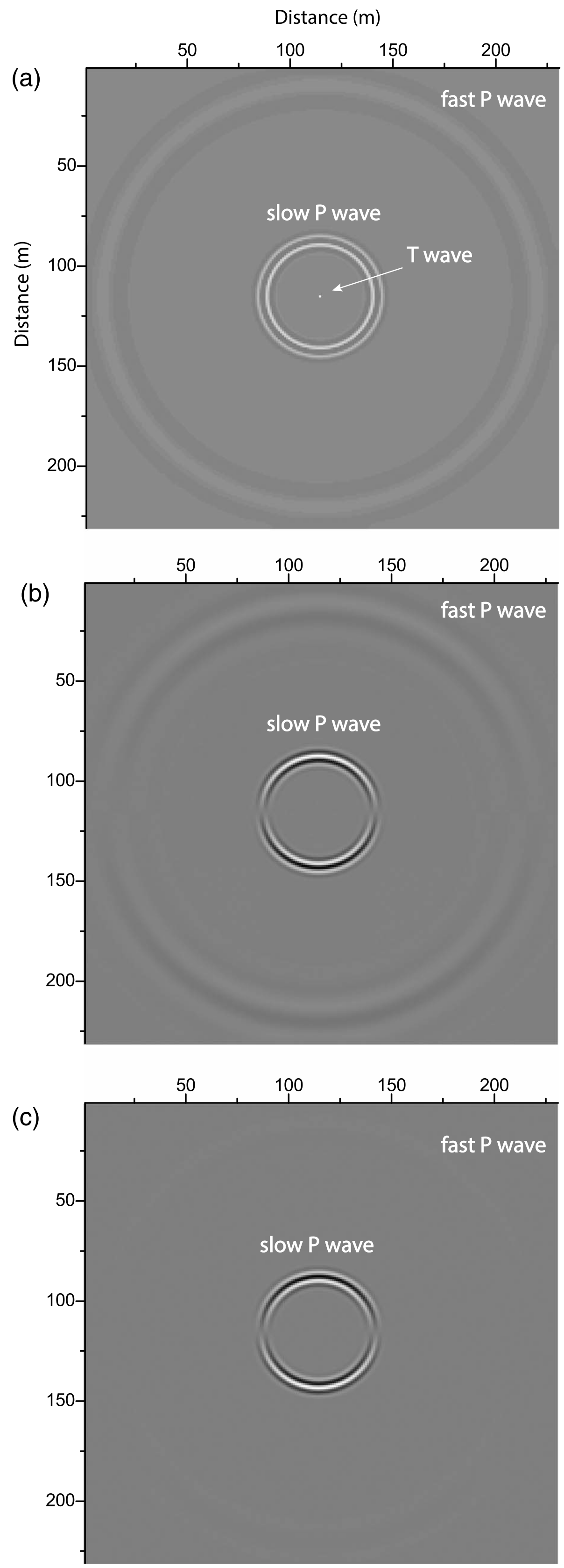

Figure 8. Snapshots of T (a), v_z (b), and q_z (c) at 47.5 ms in the coupled case, with $\eta = 0$ and dilatational sources. The properties are those of Case 1.

10.1029/2019JB017851

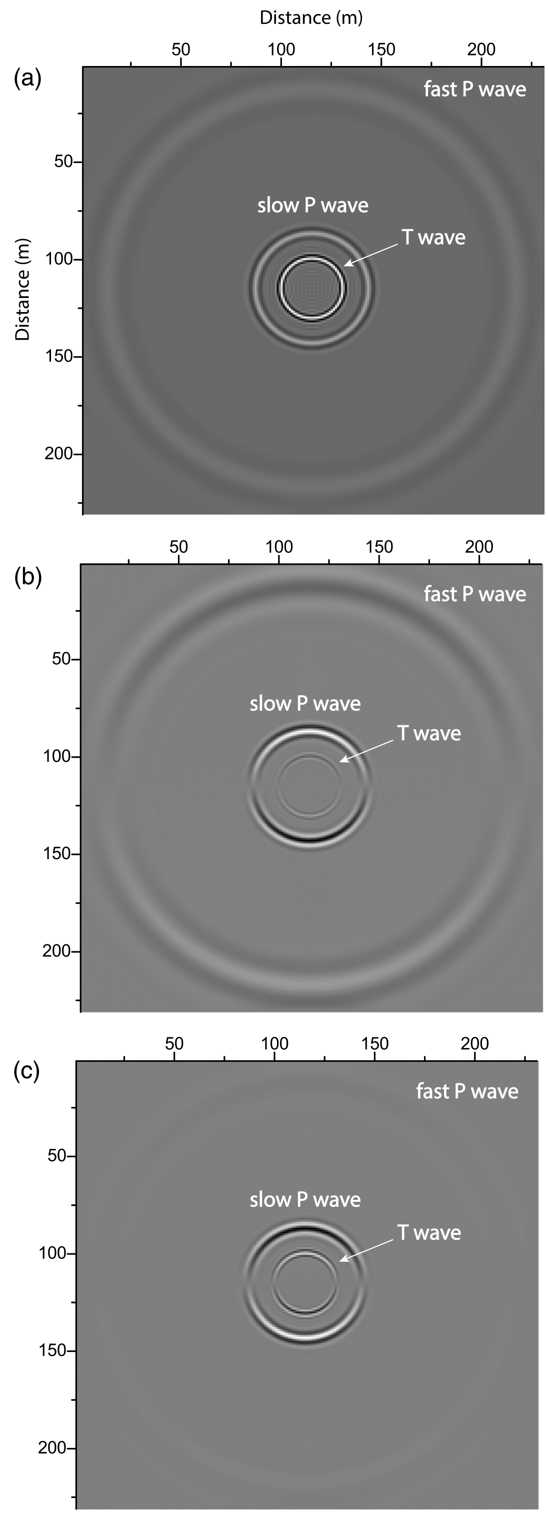

Figure 9. Snapshots of T (a), v_z (b), and q_z (c) at 47.5 ms in the coupled case, with $\eta = 0$ and a heat source. The properties are those of Case 2.

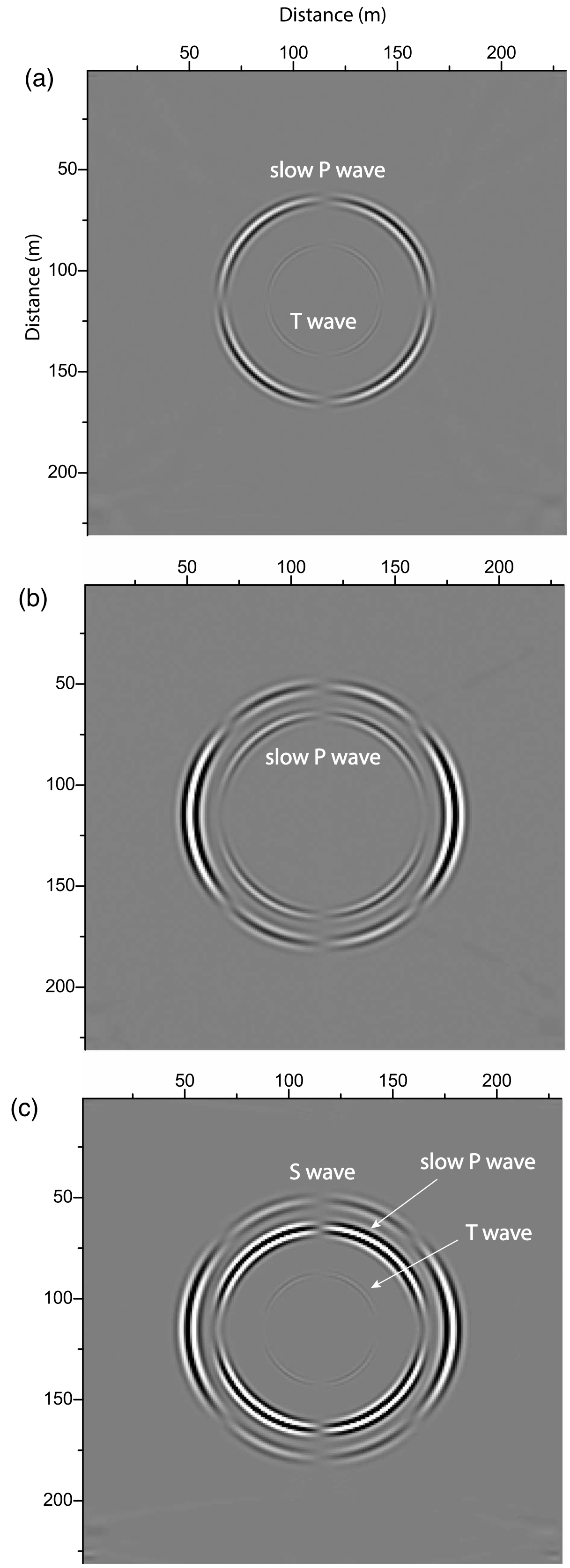

Figure 10. Snapshots of T (a), v_z (b), and q_z (c) at 75 ms in the coupled case, with $\eta = 0$ and a shear source (f_{xz}). The properties are those of Case 2.

10.1029/2019JB017851

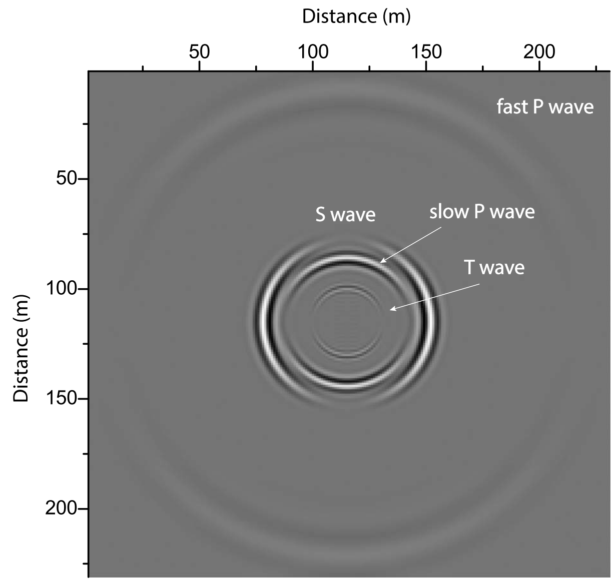

Figure 11. Snapshot of v_z at 47.5 ms in the coupled case, with $\eta = 0$ and a vertical source (f_z). The properties are those of Case 2.

propagation in homogeneous media, we show a snapshot where all the wave modes are present (Figure 11). The field has been generated by a vertical force f_z.

Finally, we present an example of an inhomogeneous medium; a plane interface separates two half spaces. The upper medium has the properties of Table 1, whereas the lower medium has $\mu_m = 9$ GPa and $K_m = 10$ GPa, that is, a higher velocity. The thermal properties are those of Case 2. We obtain snapshots of the wavefield at 55 ms, where we consider a 385×385 mesh, with $dx = dz = 1$ m. The source is dilatational ($f_{xx} = f_{zz}$), and its central frequency is 150 Hz. Figure 12 shows the snapshots of the temperature field for $\eta = 0$ (a) and $\eta \neq 0$ (b), where the wavefields are identified. The T wave is hardly affected by a variation of the dry-rock moduli. Head (lateral) waves with a planar wavefront can also be observed. Even if the heterogeneity is a simple plane interface, the wavefield is complex and could be more complex in the presence of significant S waves, generated, for instance, by a vertical elastic force.

In real geophysical cases, both the thermal wave and the Biot slow P wave are diffusive. The fact that these waves are diffusive is the cause of attenuation of the fast P wave when the medium is heterogeneous, by means of the mechanism called mesoscopic attenuation or wave-induced fluid-flow attenuation (Carcione, 2014; Müller et al., 2010; Picotti & Carcione, 2017). Energy transfer is between wave modes, with P wave to slow P (Biot) wave conversion being the main physical mechanism. The mesoscopic-scale length is intended to be larger than the grain sizes but much smaller than the wavelength of the pulse. For instance, if the matrix porosity varies significantly from point to point, diffusion of pore fluid between different regions constitutes a mechanism that can be important at seismic frequencies. In this case, there is additional loss due to P wave to thermal wave conversion, a new loss mechanism that needs to be investigated, which can be termed wave-induced thermoporoelastic attenuation in analogy with wave-induced fluid-flow attenuation. Zener (1938) explained the physics of thermoelastic attenuation in homogeneous media: “Stress inhomogeneities in a vibrating body give rise to fluctuations in temperature, and hence to local heat currents. These heat currents increase the entropy of the vibrating solid, and hence are a source of internal friction.” Basically, the temperature variation caused by the passage of the P wave provides the gradient from which the thermal dissipation and attenuation occurs. Moreover, Armstrong (1984) found that the distribution and correlation of heterogeneities play an important role in the determination of the frequency dependence of thermal dissipation, and here the wave conversion is an additional loss mechanism.

This theory and simulation can be generalized to the case of anisotropic thermoporoelasticity and a fractional heat equation. The basis for this generalization can be found in Dhaliwal and Sherief (1980), Singh and Sharma (1985), and Sherief et al. (2010) for thermoelasticity and Carcione (1996) for anisotropic poroelasticity.

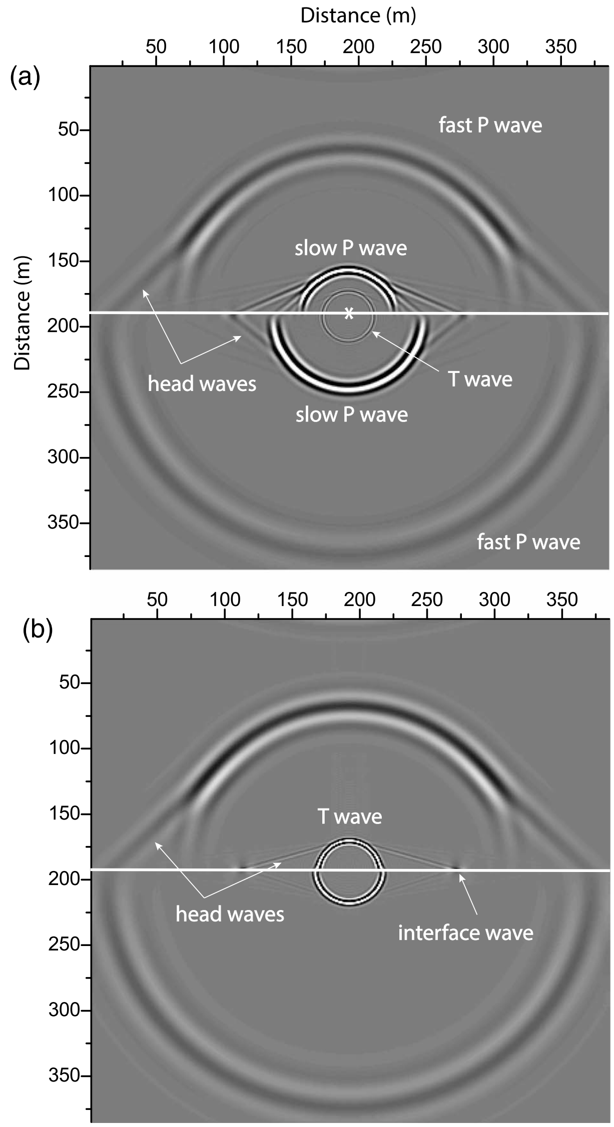

Figure 12. Snapshots of the temperature field for $\eta = 0$ (a) and $\eta \neq 0$ (b). The difference between the upper and lower media are the values of the dry-rock moduli. The whole space corresponds to Case 2.

5. Conclusions

We have proposed a numerical algorithm to solve the differential equations of dynamic porothermoelasticity, that is, wave propagation, where poroelasticity is coupled with the heat equation. The modeling algorithm is a direct-grid method that allows us to handle spatially inhomogeneous media. It is based on the Fourier method to compute the spatial derivatives and a Crank-Nicolson scheme. Another time-stepping method is based on the Runge-Kutta time-stepping technique combined with a splitting method to compute the time evolution of the wavefield.

Four waves propagate: the fast *P* wave, the slow (Biot) *P* wave, a thermal *P* wave/diffusion mode, and the *S* wave. The thermal mode is coupled with the *P* waves inducing additional energy dissipation. At low frequencies, the Biot and thermal waves are diffusive modes. The physics of wave propagation is analyzed in detail for two different sets of thermoelastic properties, and the velocities and attenuation factors of the different wave modes are determined under different conditions. The simulations show the complexity of the wavefield, which can be interpreted after a detailed study of the physics. The location of the thermoelastic and Biot relaxation peaks, describing the attenuation in the frequency axis, depend on the diffusion length of the heat and fluid flow, respectively. Future research involves the analysis of P wave dissipation in highly heterogeneous media due to thermal effects.

Appendix A: Plane Wave Analysis

To analyze the phase velocity and attenuation of the different waves modes involved in the propagation, it is enough to consider a 1-D medium, since the medium is isotropic and the S wave is not affected by the temperature effects. It can be shown that the complex velocity of the S wave is that of Biot theory:

$$v_c(S\,\text{wave}) = v_c = \sqrt{\frac{\mu}{\rho - \rho_f^2[m - \mathrm{i}\eta/(\omega\kappa)]^{-1}}} \tag{A1}$$

(e.g., Carcione, 2014, equation 7.350). In 1-D space, the field vector is $\mathbf{v} = [v, q, \sigma, p, T]^\top$, and let us consider a plane wave of the form $\exp[\mathrm{i}(\omega t - kx)]$, where ω is the angular frequency and k is the complex wavenumber. Equations (1) and (3) reduce to

$$\begin{aligned}
-k\sigma &= \omega\rho v + \omega\rho_f q, \\
kp &= \omega\rho_f v + \omega m q - (\mathrm{i}\eta/\kappa)q, \\
\omega\sigma &= -kEv - \alpha k M(\alpha v + q) - \omega\beta T, \\
\phi\omega p &= \phi k M(\alpha v + q) + \omega\beta_f T, \\
-\frac{\gamma k^2 T}{1 + \mathrm{i}\omega\tau} &= \mathrm{i}\omega c T - \mathrm{i}k T_0 \beta(v + q).
\end{aligned} \tag{A2}$$

where $E = \lambda + 2\mu$. This is a homogeneous system of linear equations whose solution is not 0 if the determinant of the system is 0. We obtain the dispersion relation for P waves:

$$a_6 v_c^6 + a_4 v_c^4 + a_2 v_c^2 + a_0 = 0, \tag{A3}$$

where

$$\begin{aligned}
a_0 &= -\mathrm{i}\omega^2\phi\gamma M E, \\
a_2 &= \omega\left(cME\phi + b\gamma\phi E_G + \beta T_0 C\right) + \mathrm{i}\omega^2\left(\gamma\phi D + \phi c M E\tau + \beta T_0 C\tau\right), \\
a_4 &= \mathrm{i}\phi b S - \omega\left(b\phi\gamma\rho + \phi c D + \phi b\tau S + T_0\beta F\right) - \mathrm{i}\omega^2\left(\phi\gamma R + \phi c\tau D + T_0\beta\tau F\right), \\
a_6 &= \phi c(\omega R V - \mathrm{i}b\rho V^*), \\
E_G &= E + \alpha^2 M, \quad C = E\beta_f + M(\alpha - 1)(\alpha\beta_f - \phi\beta), \\
D &= mE_G + \rho M - 2\alpha M\rho_f, \quad F = \beta_f(\rho - \rho_f) + \phi\beta(m - \rho_f), \\
S &= cE_G + T_0\beta^2, \quad R = m\rho - \rho_f^2, \\
V &= 1 + \mathrm{i}\omega\tau, \quad b = \frac{\eta}{\kappa}, \\
a_6 &= \phi c V\ (\omega R - ib\rho)\cdot
\end{aligned} \tag{A4}$$

If $\beta = \beta_f = 0$, we obtain a quadratic equation in v_c, corresponding to Biot velocities for the fast and slow P waves:

$$(-\mathrm{i}b\rho + \omega m\rho - \omega\rho_f^2)v_c^4 + (\mathrm{i}bE_G - \omega m E_G - \omega M\rho + 2\omega\alpha M\rho_f)v_c^2 + \omega M E = 0, \tag{A5}$$

and an additional root

$$v_c = \sqrt{\frac{\mathrm{i}\omega a^2}{1 + \mathrm{i}\omega\tau}}, \quad a = \sqrt{\frac{\gamma}{c}}, \tag{A6}$$

for the thermal wave, where a is the thermal diffusivity (Carcione, Poletto et al. 2018). This root is the solution of a telegrapher equation (e.g., Carcione & Poletto, 2002) of the form $\ddot{T} = c_\infty \Delta T + \dot{T}/\tau$, where $c_\infty = \sqrt{\gamma/(c\tau)} = a/\sqrt{\tau}$ is the velocity at infinite frequency. For $\tau = 0$, we obtain the diffusion equation and $c_\infty = \infty$. At low frequencies this velocity is 0.

The phase velocity and attenuation factor can be obtained from the complex velocity as

$$v_p = \left[\mathrm{Re}\left(v_c^{-1}\right)\right]^{-1} \quad \text{and} \quad A = -\omega\mathrm{Im}(v_c^{-1}), \tag{A7}$$

respectively (e.g., Carcione, 2014). Deresiewicz (1957) introduces the attenuation factor as the ratio of the energy dissipated per stress cycle to the total vibrational energy. It is

$$L = 4\pi \cdot \frac{Av_p}{\omega}. \tag{A8}$$

Appendix B: Crank-Nicolson Explicit Scheme

The Crank-Nicolson explicit scheme has been used by Carcione and Quiroga-Goode (1995) to solve the equations of poroelasticity and by Carcione, Poletto et al. (2018) to solve the thermoelasticity equations. The scheme, adapted to the thermoporoelasticity equations, is

$$\begin{aligned}
D^{1/2}v_x &= \beta_{11}(\sigma_{xx,x} + \sigma_{xz,z} - f_x)^n - \beta_{12}p^n_{,x} - \frac{\eta}{\kappa}\beta_{12}A^{1/2}q_x = \Pi^n_x,\\
D^{1/2}v_z &= \beta_{11}(\sigma_{xz,x} + \sigma_{zz,z} - f_z)^n - \beta_{12}p^n_{,z} - \frac{\eta}{\kappa}\beta_{12}A^{1/2}q_z = \Pi^n_z,\\
D^{1/2}q_x &= \beta_{21}(\sigma_{xx,x} + \sigma_{xz,z} - f_x)^n - \beta_{22}p^n_{,x} - \frac{\eta}{\kappa}\beta_{22}A^{1/2}q_x = \Omega^n_x,\\
D^{1/2}q_z &= \beta_{21}(\sigma_{xz,x} + \sigma_{zz,z} - f_z)^n - \beta_{22}p^n_{,z} - \frac{\eta}{\kappa}\beta_{22}A^{1/2}q_z = \Omega^n_z,\\
\epsilon_m &= (A^{1/2}v_x)_{,x} + (A^{1/2}v_z)_{,z},\\
\epsilon_f &= (A^{1/2}q_x)_{,x} + (A^{1/2}q_z)_{,z},\\
\epsilon &= \alpha\epsilon_m + \epsilon_f,\\
\dot{\epsilon}_m &= (\Pi^n_x)_{,x} + (\Pi^n_z)_{,z},\\
\dot{\epsilon}_f &= (\Omega^n_x)_{,x} + (\Omega^n_z)_{,z},\\
\Delta_\gamma T^n &= c(A^{1/2}\psi + \tau D^{1/2}\psi) + \beta T_0[(\epsilon_m + \tau\dot{\epsilon}_m) + (\epsilon_f + \tau\dot{\epsilon}_f)] + q^n,\\
T^{n+1} &= T^n + dt \quad \psi^{n+1/2},\\
D^1\sigma_{xx} &= 2\mu(A^{1/2}v_x),x + \lambda\epsilon_m + \alpha M\epsilon - \beta A^{1/2}\psi + f_{xx},\\
D^1\sigma_{zz} &= 2\mu(A^{1/2}v_z),z + \lambda\epsilon_m + \alpha M\epsilon - \beta A^{1/2}\psi + f_{zz},\\
D^1\sigma_{xz} &= \mu[(A^{1/2}v_x),z + (A^{1/2}v_z),x)] + f_{xz},\\
\phi D^1 p &= -\phi M\epsilon + \beta_f A^{1/2}\psi - f_f,
\end{aligned} \tag{B1}$$

where

$$D^j\phi = \frac{\phi^{n+j} - \phi^{n-j}}{2j\,dt} \quad \text{and} \quad A^j\phi = \frac{\phi^{n+j} + \phi^{n-j}}{2} \tag{B2}$$

are the central differences and mean value operators, based on a Crank-Nicolson (staggered) scheme (Jain, 1984, p. 269) for the particle velocities. In this three-level scheme, $(v_x, v_z, q_x, q_z, \psi)$ at time $(n + 1/2)dt$ and stresses and temperature at time $(n + 1)dt$ are computed explicitly from $(v_x, v_z, q_x, q_z, \psi)$ at time $(n - 1/2)dt$ and stresses and temperature at time $(n - 1)dt$ and ndt, respectively.

The tenth equation (B1) above yields

$$\begin{aligned}
(dt + 2\tau)\psi^{n+1/2} = \frac{2dt}{c}&[\Delta_\gamma T^n - \beta T_0[(\epsilon_m + \tau\dot{\epsilon}_m) + (\epsilon_f + \tau\dot{\epsilon}_f)]\\
&- q^n] - (dt - 2\tau)\psi^{n-1/2}.
\end{aligned} \tag{B3}$$

The stability analysis has been performed in Carcione and Quiroga-Goode (1995), that is, a Von Neumann stability analysis based on the eigenvalues of the amplification matrix (Jain, 1984, p. 418). The algorithm has first-order accuracy but possesses the stability properties of implicit algorithms, and the solution can be obtained explicitly.

Appendix C: Splitting algorithm

The eigenvalues of $\mathbf{M}$ in equation (10) may have negative real parts and differ greatly in magnitude. This problem is due to the presence of the viscosity/permeability term in Biot's equation and the relaxation time in the heat equation. The presence of large eigenvalues, together with small eigenvalues, indicates that the problem is stiff. Moreover, the presence of real positive eigenvalues can induce instability in the time-stepping method. To solve these problems, the differential equations are solved with the splitting algorithm used by Carcione and Quiroga-Goode (1995), Carcione (1996), and Carcione and Seriani (2001). The propagation matrix can be partitioned as

$$\mathbf{M} = \mathbf{M}_r + \mathbf{M}_s, \tag{C1}$$

where subscript r indicates the regular matrix, and subscript s denotes the stiff matrix, involving the quantity γ and the coupling terms. The evolution operator can be expressed as $\exp(\mathbf{M}_r + \mathbf{M}_s)t$. It is easy to show that the product formula

$$\exp(\mathbf{M}dt) = \exp\left(\frac{1}{2}\mathbf{M}_s dt\right)\exp(\mathbf{M}_r dt)\exp\left(\frac{1}{2}\mathbf{M}_s dt\right) \tag{C2}$$

is second-order accurate in dt. Equation (C2) allows us to solve the unstable equations separately. From equations (6) and (9), these are

$$\begin{aligned}
&\dot{v}_x = -\frac{\eta}{\kappa}\beta_{12}q_x, \qquad \dot{v}_z = -\frac{\eta}{\kappa}\beta_{12}q_z,\\
&\dot{q}_x = -\frac{\eta}{\kappa}\beta_{22}q_x, \qquad \dot{q}_z = -\frac{\eta}{\kappa}\beta_{22}q_z,\\
&\dot{\sigma}_{xx} = -\beta\psi, \qquad \dot{\sigma}_{zz} = -\beta\psi, \qquad \phi\dot{p} = \beta_f\psi, \qquad \dot{\psi} = -\frac{1}{\tau}\psi.
\end{aligned} \tag{C3}$$

These equations can be solved analytically, giving

$$\begin{aligned}
&{v_x}^* = {v_x}^n + \frac{\beta_{12}}{\beta_{22}}[\exp(\lambda_s dt) - 1]{q_x}^n, \qquad {v_z}^* = {v_z}^n + \frac{\beta_{12}}{\beta_{22}}[\exp(\lambda_s dt) - 1]{q_z}^n,\\
&{q_x}^* = \exp(\lambda_s dt){q_x}^n, \qquad {q_z}^* = \exp(\lambda_s dt){q_z}^n,\\
&\sigma^*_{xx} = \sigma^n_{xx} + \tau\beta\left[\exp(-dt/\tau) - 1\right]\psi^n, \qquad \sigma^*_{zz} = \sigma^n_{zz} + \tau\beta\left[\exp(-dt/\tau) - 1\right]\psi^n,\\
&p^* = p^n - \frac{\tau\beta_f}{\phi}\left[\exp(-dt/\tau) - 1\right]\psi^n,\\
&\psi^* = \exp(-dt/\tau)\psi^n,
\end{aligned} \tag{C4}$$

where $\lambda_s = -(\eta/\kappa)\beta_{22}$. Note that when $\eta = 0$, is $v^* = v^n$ and $q^* = q^n$, giving the purely elastic problem.

The intermediate vector

$$\mathbf{W}^* = [{v_x}^*, {v_z}^*, {q_x}^*, {q_z}^*, \sigma^n_{xx}, \sigma^n_{zz}, \sigma^n_{xz}, p^n, T, \psi^*]^\top \tag{C5}$$

is the input for an explicit high-order scheme that solves the system of equations with $\eta = 0$ to give $\mathbf{W}^{n+1}$.

The regular operator $\exp(\mathbf{M}_r dt)$ is approximated with a fourth-order Runge Kutta solver. The output vector is

$$\mathbf{v}^{n+1} = \mathbf{v}^* + \frac{dt}{6}(\Delta_1 + 2\Delta_2 + 2\Delta_3 + \Delta_4), \tag{C6}$$

where

$$\begin{aligned}
&\Delta_1 = \mathbf{M}_r\mathbf{v}^* + \mathbf{s}^n,\\
&\Delta_2 = \mathbf{M}_r\left(\mathbf{v}^* + \frac{dt}{2}\Delta_1\right) + \mathbf{s}^{n+1/2},\\
&\Delta_3 = \mathbf{M}_r\left(\mathbf{v}^* + \frac{dt}{2}\Delta_2\right) + \mathbf{s}^{n+1/2},\\
&\Delta_4 = \mathbf{M}_r(\mathbf{v}^* + dt\Delta_3) + \mathbf{s}^{n+1},
\end{aligned}$$

and $\mathbf{v}^*$ is the intermediate output vector obtained after the operation with the stiff evolution operator. Then, ψ^* is input to a Runge-Kutta fourth-order time-stepping algorithm (involving matrix $\mathbf{M}_r$), and the spatial derivatives are calculated with the Fourier method by using the fast Fourier transform (Carcione, 2014). This spatial approximation is infinitely accurate for band-limited periodic functions with cutoff spatial wavenumbers which are smaller than the cutoff wavenumbers of the mesh. Due to the splitting algorithm, the modeling is second-order accurate in the time discretization.

Acknowledgments
The authors are grateful to the Editors and reviewers for their valuable comments. This work is supported by the Specially-Appointed Professor Program of Jiangsu Province, China, and the Fundamental Research Funds for the Central Universities, China Data of wave propagation of the associated temperature field in this article can be accessed at the website (https://zenodo.org/record/3241814).

References

Armstrong, B. H. (1984). Models for thermoelastic in heterogeneous solids attenuation of waves. *Geophysics*, *49*, 1032–1040.

Biot, M. A. (1956). Thermoelasticity and irreversible thermodynamics. *Journal of Applied Physics*, *27*, 240–253.

Biot, M. A. (1962). Mechanics of deformation and acoustic propagation in porous media. *Journal of Applied Physics*, *33*, 1482–1498.

Bonafede, M. (1991). Hot fluid migration: An efficient source of ground deformation: Application to the 1982–1985 crisis at Campi Flegrei-Italy. *Journal of Volcanology and Geothermal Research*, *48*, 187–198.

Carcione, J. M. (1996). Wave propagation in anisotropic, saturated porous media: Plane wave theory and numerical simulation. *Journal of the Acoustical Society of America*, *99*(5), 2655–2666.

Carcione, J. M. (2014). Wave fields in real media. Theory and numerical simulation of wave propagation in anisotropic, anelastic, porous and electromagnetic media. Elsevier (Third edition, extended and revised).

Carcione, J. M., & Poletto, F. (2002). A telegrapher equation for electric telemetering in drill strings. *IEEE Transactions On Geoscience and Remote Sensing*, *40*, 1047–1053.

Carcione, J. M., Poletto, F., Farina, B., & Bellezza, C. (2018). 3D seismic modeling in geothermal reservoirs with a distribution of steam patch sizes, permeabilities and saturations, including ductility of the rock frame. *Physics of the Earth and Planetary Interiors*, *279*, 67–78.

Carcione, J. M., & Quiroga-Goode, G. (1995). Some aspects of the physics and numerical modeling of Biot compressional waves. *Journal of Computational Acoustics*, *3*, 261–280.

Carcione, J. M., & Seriani, G. (2001). Wave simulation in frozen porous media. *Journal of Computational Physics*, *170*, 676–695.

Carcione, J. M., Wang, Z.-W., Ling, W., Salusti, E., Ba, J., & Fu, L.-Y. (2018). Simulation of wave propagation in linear thermoelastic media. *Geophysics*, *84*, T1–T11. https://doi.org/10.1190/geo2018-0448.1

Cattaneo, C. (1958). Sur une forme de l'équation de la chaleur éliminant paradoxe d'une propagation instantanée. *Comptes rendus de l'Académie des Sciences Journal (Paris)*, *247*, 431–433.

Deresiewicz, H. (1957). Plane waves in a thermoelastic solid. *Journal of the Acoustical Society of America*, *29*, 204–209.

Dhaliwal, R. S., & Sherief, H. H. (1980). Generalized thermoelasticity for anisotropic media. *Quarterly of Applied Mathematics*, *38*, 1–8.

Fu, L.-Y. (2012). Evaluation of sweet spot and geopressure in Xihu (Sag. Tech. Report, CCL2012-SHPS-0018ADM): Key laboratory of petroleum resource research, Institute of Geology and Geophysics, Chinese Academy of Sciences.

Fu, L.-Y. (2017). Deep-Superdeep Oil & Gas Geophysical Exploration 111. Program report jointly initiated by MOE and SAFEA, B18055. School of Geosciences, China University of Petroleum (East China).

Iesan, D., & Quintanilla, R. (2014). On a theory of thermoelastic materials with a double porosity structure. *Journal of Thermal Stresses*, *37*, 1017–1036.

Jacquey, A. B., Cacace, M., Blöcher, G., & Scheck-Wenderoth, M. (2015). Numerical investigation of thermoelastic effects on fault slip tendency during injection and production of geothermal fluids. *Energy Procedia*, *76*, 311–320.

Jain, M. K. (1984). Numerical solutions of partial differential equations. Wiley Eastern Ltd.

Kumar, R., Vohra, R., & Gorla, M. G. (2017). Variational principle and plane wave propagation in thermoelastic medium with double porosity under Lord-Shulman theory. *Journal of Solid Mechanics*, *9*, 423–433.

Lord, H., & Shulman, Y. (1967). A generalized dynamical theory of thermoelasticity. *Journal of the Mechanics and Physics of Solids*, *15*, 299–309.

Maxwell, J. C. (1867). On the dynamic theory of gases. *Philosophical Transactions of the Royal Society London*, *157*, 49–88.

McTigue, D. F. (1986). Thermoelastic response of fluid-saturated porous rock. *Journal of Geophysical Research*, *91*(B9), 9533–9542.

Müller, T. M., Gurevich, G., & Lebedev, M. (2010). Seismic wave attenuation and dispersion resulting from wave-induced flow in porous rocks—A review. *Geophysics*, *75*(5), 75,A147–75,A164.

Nield, D. A., & Bejan, A. (2006). *Convection in Porous Media* (third ed.). Berlin: Springer.

Noda, N. (1990). Thermal stress problem in a fluid-filled porous circular cylinder. *Zeitschrift fur Angewandte Mathematik und Mechanik*, *70*, 543–549.

Picotti, S., & Carcione, J. M. (2017). Numerical simulation of wave-induced fluid flow seismic attenuation based on the Cole-Cole model. *Journal of the Acoustical Society of America*, *142*, 134–145. https://doi.org/10.1121/1.4990965

Reza Eslami, M., Hetnarski, R. B., Ignazak, J., Noda, N., Sumi, N., & Tanigawa, Y. (2013). Theory of elasticity and thermal stresses. In *Solid Mechanics and Applications* (Vol. 197): Springer.

Rudgers, A. J. (1990). Analysis of thermoacoustic wave propagation in elastic media. *Journal of the Acoustical Society of America*, *88*(2), 1078–1094.

Sharma, M. D. (2008). Wave propagation in thermoelastic saturated porous medium. *Journal of Earth System Science*, *117*, 951–958.

Sherief, H. H., El-Sayed, A. M. A., & Abd El-Latief, A. M. (2010). Fractional order theory of thermoelasticity. *International Journal of Solids and Structures*, *47*, 269–275.

Singh, H., & Sharma, J. N. (1985). Generalized thermoelastic waves in transversely isotropic media. *Journal of the Acoustical Society of America*, *77*, 1046–1053.

Treitel, S. (1959). On the attenuation of small-amplitude plane stress waves in a thermoelastic solid. *Journal of Geophysical Research*, *64*, 661–665.

Vernotte, P. (1948). Théorie continue et théorie moléculaire des phénomènes thermocinétiques. *Comptes rendus de l'Académie des Sciences (Paris)*, *227*, 43–44.

Zener, C. (1938). Internal friction in solids. II. General theory of thermoelastic internal friction. *Physical Review*, *53*, 90–99.

Erratum

In the originally published version of this article, the final line of equation (A4) was omitted: $a_6 = \phi cV\ (\omega R - ib\rho)\cdot$ Additionally, the term σ_{zz} in the fourth line of equation B1 was incorrectly given as τ_{zz} in the originally published version. These errors have been corrected, and this may be considered the official version of record.